

Influence of synthetic inclusions on the degradation and deformation of ballast under heavy-haul cyclic loading

Authors: Trung Ngo^a, Buddhima Indraratna^{b*}, Fernanda Ferreira^c

^aSenior Lecturer, Transport Research Centre, School of Civil and Environmental Engineering, University of Technology Sydney, 15 Broadway, Ultimo NSW 2007, Australia. Email: Trung.Ngo@uts.edu.au

^bDistinguished Professor of Civil Engineering and Director, Transport Research Centre, University of Technology Sydney 15 Broadway, Ultimo, NSW 2007, Australia; Founding Director, ARC Industrial Transformation Training Centre for Advanced Technologies in Rail Track Infrastructure (ITTC-Rail), University of Wollongong, NSW 2522, Australia. Email: Buddhima.Indraratna@uts.edu.au

^cPostdoctoral Researcher, CONSTRUCT, Faculty of Engineering, University of Porto, 4200-465 Porto, Portugal. Email: fbf@fe.up.pt

Abstract:

This study investigates the benefits of artificial inclusions placed underneath the ballast layer. A series of large-scale cyclic triaxial tests were carried out on ballast with and without these inclusions under 25-tonne and 35-tonne axle loads and frequencies of $f=15$ Hz and 25 Hz, using a Process Simulation Prismatic Triaxial Apparatus. The laboratory results show that a geogrid installed between the ballast and capping layer decreases both deformation and degradation of the aggregates, which can be attributed to enhanced internal confinement and restricted particle movement. Laboratory tests also showed that placing a rubber mat underneath the ballast layer significantly reduced ballast breakage. A numerical model using the discrete element method (DEM) was developed and validated against the experimental observations. The DEM model was utilised to explore the contact forces that developed across the granular assemblies, and to study the interaction between aggregates and the synthetic inclusions from a particle-level perspective.

Keywords: *Ballast, geogrids, rubber mats, cyclic loading, rail geotechnics*

1. Introduction

Current Australian rail transportation infrastructure is in urgent need to be upgraded to support increasing volumes of freight, especially in the agricultural and mining sectors. The ballast layer of conventional ballasted tracks transmits and distributes train loads to underlying layers at reduced levels of stress [1]. Repeated train loads cause the ballast to deteriorate and spread laterally, which adversely affects the safety and efficiency of railway tracks [1-5]. Impact forces induced by rail corrugations, wheel flats, dipped rails, defective rail welds, or variations in the track foundation stiffness at transition zones such as bridge approaches, can exacerbate the rate of track degradation

and lead to more frequent maintenance operations [6-13]. In practice, a large proportion of track maintenance costs are related to substructure problems such as ballast breakage, poor drainage, differential settlements, and track buckling [8,14,15].

The use of geosynthetic products such as geogrids, geocomposites, and geotextiles in new rail tracks and track rehabilitation has gained wide acceptance worldwide owing to its technical, economic, and environmental benefits [16-20]. When properly designed and installed, geosynthetics are a cost-effective alternative to more traditional solutions [4,21-24]. Recent studies have shown that geogrids in rail tracks can attenuate the rate of permanent ballast deformation and particle breakage under repetitive wheel loads [22,25-28]. Walls and Galbreath [29] observed that rail tracks laid on soft subgrade are prone to excessive track settlements, but the settlement can be decreased significantly with geogrid reinforcement. Similarly, Hornicek et al. [30] concluded that geogrid inserted directly under the ballast layer helps to reduce its settlement. Esmaeili et al. [31] examined the way geogrids improve the stability of tracks and found that geogrid-reinforced embankments experienced a 7.14% higher bearing capacity and an 11.24% reduction in settlement. An appropriately selected geogrid locks the ballast particles within its apertures restricting their lateral movement and vertical settlement [26,32-38]. Although it is widely recognised that geogrids strengthen the track substructure, the exact role of the interface between ballast and different geogrids (varying aperture sizes and shapes) has not been examined in detail for changing the current technical standards applied to rail tracks. In addition, there has been limited attempt to examine how a combination of geogrid and recycled rubber mat would increase track stability under cyclic loading conditions.

Current literature indicates that only a few studies have examined the interactions at the ballast-geogrid interfaces using numerical methods [27,39-44], because these mechanisms are complex and depend on the type of geogrid (geometrical and mechanical properties of the reinforcements), the nature of the ballast/capping layer, and the induced dynamic loads in an actual track environment, among others. It is therefore necessary to extend our current knowledge by developing a computational model for design and analysis that has been calibrated and validated against prototype large-scale laboratory tests.

The main aim of this study is to investigate the potential use of geogrids and recycled rubber mats to simultaneously control both deformation and degradation of ballasted tracks and to enhance track performance under heavy-haul cyclic loading. While the use of a geogrid or a rubber mat as separate components has been investigated in a few past studies, there has been limited attempts to examine how a combination of geogrid and rubber mat would enhance track stability. To this end, a series of large-scale laboratory tests using the Process Simulation Prismoïdal Triaxial Apparatus (PSPTA) was carried out under different cyclic loadings and frequencies. A new device, a Pile Driving Monitor

(PDM), was used to record the track displacements during testing in tandem with a novel Stress Sensing Sheet (SSS) that was inserted within the substructure to detect stress concentrations. A numerical analysis using the discrete element method (DEM) was then performed considering a given number of loading cycles to investigate the interface behaviour and interaction between geogrid and ballast particles at the micro-mechanical level. Details of the methodology used and the associated results are presented in the following sections.

2. Large-scale laboratory testing

2.1. Process Simulation Prismoidal Triaxial Apparatus

A large-scale Process Simulation Prismoidal Triaxial Apparatus (PSPTA) with a high-frequency dynamic actuator and that can accommodate 800 mm × 800 mm × 600 mm size samples was used in the laboratory study (Figure 1a). The test chamber mimics the unit cell area of a standard gauge Australian heavy haul track, so it can realistically simulate the stresses and appropriate boundary conditions. Unlike most conventional geotechnical rigs with fixed boundaries, the PSPTA has moveable walls that allow lateral displacements to occur in the transverse and longitudinal directions, while the required confining pressure is applied by hydraulic jacks at the boundaries. Cyclic loads are applied directly onto a sleeper-rail assembly by a servo-hydraulic actuator (Figure 1b), and they are recorded by a load cell (capacity: 1000 kPa) attached to the actuator. The rail is directly connected to the concrete sleeper and there is no rail pad between the rail and the sleeper. During these tests, the lateral and vertical deformation of ballast are measured at specific numbers of cycles. After completing the prescribed number of load cycles, the ballast aggregates are sieved to obtain the final particle size distribution and quantify the amount of breakage induced by cyclic loading.

2.2. Instrumentation

The instrumentation used for the laboratory tests included settlement pegs, pressure cells, potentiometers, LVDTs, a Pile Driving Monitor - PDM (Figure 1a) and a Stress Sensing Sheet (SSS). Eight settlement pegs were placed over the compacted capping and ballast layers to measure the settlement induced by cyclic loading. Two displacement sensors were mounted onto the sleeper surface (i.e., near the left and right ends of the sleeper) to ensure that the sleeper settled down evenly during the tests. Two pressure plates (200 mm diameter by 20 mm thick) with a capacity of 1 MPa were used to measure the vertical stresses in the ballast assembly. The lateral deformations of ballast were determined based on the displacements of the vertical walls that were recorded by LVDTs. A Stress Sensing Sheet (SSS) was installed under the ballast layer to investigate the effect the inclusions

had on the concentration of stresses in the ballast. A Pile Driving Monitor (PDM) was also used to record the vertical displacement of the rail-sleeper assembly during the tests. This PDM has the latest optoelectronic technology so it can make non-contact measurements of vertical displacement under static or dynamic loading conditions. The device includes a reflector that was glued onto the rail, as shown in Figure 1b, and it was set up at a distance of about 4 m from the target.

2.3. Materials and test program

The materials used in this study were conventional track substructure materials such as capping (sub-ballast), ballast, and three different artificial inclusions: a geogrid (GGR), a geocomposite reinforcement (GCR) and a recycled rubber mat (RM). The GGR was a laid and welded biaxial geogrid composed of flat polypropylene bars with 31×31 mm square apertures, whereas the GCR was a geocomposite reinforcement consisting of a similar biaxial geogrid attached to a polypropylene nonwoven geotextile. The RM was a 10 mm thick planar mat manufactured from waste tyres. The physical and mechanical properties of these artificial inclusions are summarised in Table 1.

A 180 mm thick capping layer (sub-ballast) consisting of a sand-gravel mixture was compacted towards the bottom of the test chamber in two sub-layers to achieve a unit weight of 19.5 kN/m³ (Figure 2a). In the tests involving artificial inclusions, these materials were installed over the compacted capping (Figure 2b). The fresh ballast aggregates from Bombo quarry, New South Wales, Australia were cleaned and sieved according to the Australian Standard AS 2758.7:2015 [45]. The ballast aggregates were compacted in 3 sub-layers (100 mm thick) to a bulk density of 15.8 kN/m³, up to a total thickness of 300 mm (Figure 2c), and this bulk density was kept identical in all specimens to capture realistic Australian track conditions. It should be noted that the ballast grains in each sub-layer were painted in different colours to enable estimating the respective amount of degradation (breakage), as well as identifying the sizes of ballast aggregates that were more prone to breakage. A rail-sleeper assembly was placed on top of the load-bearing ballast and surrounded by additional ballast aggregates to simulate the crib ballast (Figure 2d). The particle size distributions of the capping and ballast materials used in these tests are shown in Fig. 3, and follow the Australian Rail Track Corporation (ARTC) guidelines [46], as well as the AS 2758.7:2015 [45].

A series of tests with and without the artificial inclusions was carried out to examine the role of geosynthetics and recycled rubber mat in relation to the deformation and degradation (breakage) of ballast under heavy-haul cyclic loading. The test program is shown in Table 2; it includes 8 tests carried out under different load frequencies ($f = 15\text{Hz}$ and 25Hz) and axle loads ($F_{axle_load} = 25\text{-tonne}$ and 35-tonne). Every test was subjected to $N=500,000$ loading cycles under a lateral confining

pressure of 15 kPa in the transverse direction parallel to the sleeper. After each test, the ballast aggregates in each layer were sieved separately to quantify the amount of ballast breakage.

3. Results and discussion of the laboratory tests

3.1. Permanent lateral and vertical strains of ballast

Figure 4 shows the evolution of lateral and vertical strains of ballast with and without the inclusion of GGR and RM. As expected, ballast aggregates were compressed and hence displaced laterally under the applied cyclic loadings. The lateral strains (ε_3) were estimated based on the total lateral displacements of the two side walls (transverse walls) of the test chamber. The vertical strains (ε_1) were determined based on the average readings of the settlement pegs installed at the capping layer and top surface of ballast. It is noted that the geogrid significantly reduced the lateral and vertical deformation of the ballast. In fact, when ballast grains are compacted over a geogrid they penetrate through the reinforcement apertures to create a mechanical interlock between the geogrid and surrounding ballast aggregates. This interlocking effect enables the geogrid to act like a non-horizontal displacement boundary that confines and restrains the ballast from free movement, reducing their permanent deformations. The combination of a geogrid and a rubber mat (test T8) resulted in the least amount of deformation due to the interlocking effect promoted by the GGR, along with the energy absorbing capacity of the rubber mat (RM). Hence, less energy was transferred to the ballast, thereby attenuating its deformation. The lateral and vertical strains increased rapidly during the initial loading stages ($N=10,000$ cycles) due to the initial densification of the ballast layer and the abrasion and attrition of sharp angular ballast particles, but this rate of strain accumulation (ε_1 , ε_3) gradually decreased at subsequent loading cycles. During the period of rapid deformation, the ballast assembly became denser, and thus the potential of particle rearrangement slowly decreased until the ballast reached a relatively stable condition.

The volumetric strain (ε_{vol}) and shear strain (ε_s) of the ballast layer were calculated based on the vertical and lateral strains, as given by:

$$\varepsilon_{vol} = \varepsilon_1 + \varepsilon_2 + \varepsilon_3 \quad (1)$$

$$\varepsilon_s = \frac{\sqrt{2}}{3} \left\{ \sqrt{(\varepsilon_1 - \varepsilon_2)^2 + (\varepsilon_2 - \varepsilon_3)^2 + (\varepsilon_1 - \varepsilon_3)^2} \right\} \quad (2)$$

The volumetric strain (ε_{vol}) and shear strain (ε_s) of ballast subjected to different axle loads and frequencies are shown in Figure 5. Note that while an increasing axle load and/or frequency led to an

increment in the accumulation of ε_{vol} and ε_s , geogrids helped to reduce these strains significantly. The geogrid reduced the ε_{vol} by about 19%-33% and the ε_s from approximately 17.2% to 29.1%. Under a high frequency of $f=25$ Hz ($F_{axle}=25$ tonne) and without any artificial inclusion (test T5), the ballast grains exhibited the highest volumetric strain (ε_{vol}) and shear strain (ε_s) of about 13.5% and 10.1%, but with a geogrid inclusion (test T6) the ε_{vol} and ε_s were decreased to 11.8% and 8.4%, respectively.

3.2. Real time track displacements using a Pile Driving Monitor

A Pile Driving Monitor (PDM) was used to validate the settlement of ballast under cyclic loading, as shown earlier in Figure 1. Figure 6 shows the vertical displacements of the rail during a cyclic test (up to $N=10,000$ cycles) obtained through the PDM (test T2). The test T2 (subjected to 25 tonne-axle load and loading frequency of 15 Hz) is chosen for real-time track displacement measurement since it represents typical Australian freight trains travelling at about 60-80km/h on standard gauge tracks [47]. The settlements captured by the PDM are comparable to those measured by the settlement pegs during the cyclic loading tests. The ballast assembly settled rapidly during the first 1000 cycles as the ballast aggregates were rearranged and re-oriented, but then the rate of settlement decreased as the test progressed to a larger number of cycles and the ballast matrix became denser.

3.3. Measuring the resilient modulus of ballast

The resilient modulus (M_R) is a key parameter for the design and analysis of track substructure under repeated wheel loading. M_R can be defined by the ratio of the applied cyclic deviator stress ($\Delta q_{cyc} = q_{cyc,max} - q_{cyc,min}$) to the recoverable (resilient) axial strain, $\varepsilon_{1,rec}$ during a loading-unloading cycle.

$$M_R = \frac{\Delta q_{cyc}}{\varepsilon_{1,rec}} = \frac{q_{cyc,max} - q_{cyc,min}}{\varepsilon_{1,rec}} \quad (3)$$

During the tests, data bursting commenced at pre-determined loading cycles (N) to calculate the corresponding resilient modulus, M_R ($N = 1, 50, 100, 500, 1000, 5000, 10000, 50000, 100000, 200000, 300000, 400000, 500000$). The typical applied cyclic stress-axial strain curves obtained from these tests are shown in Figure 7a. It is measured that the area of hysteresis loops becomes smaller with an increased N , indicating that the granular layer gets more compacted and responds more elastically toward the end of the test. The variations of M_R values calculated under various loadings and frequencies ($f = 15\text{Hz}, 25\text{Hz}$) shown in Figure 7b reveal a large increase in M_R within the first $N=100,000$ cycles as the aggregates rapidly densified; this is associated with an increase in the overall stiffness of the assembly. The subsequent increase in M_R became marginal because the ballast grains

were in more stable condition, leading to a reduced increment rate of M_R . For a given applied loading and frequency, the inclusion of GGR resulted in an increase in the resilient modulus of ballast (M_R), since the interlock between the geogrid and the aggregates contributed to increased stiffness of the composite material.

3.4. Role of inclusions in decreasing ballast breakage

After each test, the ballast from each layer was recovered separately (top, middle and bottom layers) and then passed through the standard sieves to estimate the extent of breakage. As shown in Figure 8a, ballast aggregates experienced different types of degradation (attrition, corner breakage, abrasion) when subjected to cyclic loads. The role of geogrids and rubber mat in reducing the degradation of ballast was analysed by quantifying and comparing, for the different test conditions, the shift in the particle size distribution (PSD) curve of ballast towards smaller particles due to breakage, as introduced by Indraratna et al. [48]. By recognising this shift as the degradation indicator, the ballast breakage index (BBI) can be calculated as:

$$BBI = \frac{A}{A + B} \quad (4)$$

where, A is the shift in PSD due to ballast breakage (i.e. the area between the initial and final PSD curves), and B is the potential breakage or the area between the arbitrary boundary of maximum breakage and the final particle size distribution. Note that the BBI has a lower limit of 0 (no breakage) and an upper limit of 1. A summary of ballast breakage measured with and without geogrid and rubber mat subjected to different cyclic loading conditions is tabulated in Table 3. The percentage reduction in the ballast breakage index, R_{BBI} (%) attributed to the effects of the artificial inclusions was determined as:

$$R_{BBI}(\%) = \frac{BBI_{unreinforced} - BBI_{reinforced}}{BBI_{unreinforced}} \times 100 \quad (5)$$

The BBI values obtained after different tests are presented in Figure 8b; they indicate that the ballast in the top layer experienced the highest breakage, which is associated with the high interparticle contact stresses and hard interfaces with the concrete sleeper. With geogrid inclusion, there was a considerable decrease in the BBI as the ballast particles interlocked within the geogrid apertures, which in turn reduced the movement of particles and the extent of attrition-based degradation. A combination of geogrid and rubber mat (test T8) led to the largest reduction in ballast breakage ($R_{BBI} = 17.74\%$) with respect to the value obtained in the absence of reinforcement (test T1), whereas the geogrid (test T2) and geocomposite (test T7) reduced ballast breakage to a lower extent ($R_{BBI} = 8.06\%$

and $R_{BBI} = 6.45\%$, respectively), as indicated in Table 3. It is believed that the elasticity of rubber mats absorbs a certain amount of the kinetic energy generated by cyclic loading, so less energy is transferred to the ballast grains, which is why the ballast experiences less breakage. In fact, the rubber mats can store energy through elastic strain energy when the cyclic loading is continually applied, and once the train loading is removed most of that stored energy will be released to the ballast and sub-ballast sandwiching the mat. However, with increasing number of cycles over time, this ability to store and release will diminish as these recycled rubber sheets can lose their elastic resilience (i.e. plastic damage). In practice, a reduction in ballast degradation by the inclusion of geogrid and rubber mat would represent significantly extended ballast lifetime, and hence contribute to extended maintenance cycles with associated major economic and environmental benefits.

3.5. Measured stress distributions

The pressure cells at the sleeper-ballast interface and at the bottom of the ballast layer were designed to measure the vertical stresses (σ_v) acting at different depths. Figure 9 shows the distribution of vertical stresses in the ballast assembly for different tests recorded at $N=100,000$ cycles. The vertical stress measurements from Australian tracks located in the towns of Singleton and Bulli are also plotted in Figure 9 for comparison purposes [49]. The vertical stress σ_v decreased with the depth of the test chamber where the values of σ_v recorded at the capping layer were approximately 95 kPa and 210 kPa under 25-tonne and 35-tonne axle loads, respectively. As expected, the geogrid-reinforced ballast (i.e. reinforcement placed at the interface between the ballast and capping layers) reduced the stresses more effectively than the unreinforced ballast assembly, because the geogrid provided a stiffer interface as the ballast grains interlocked. This action facilitated an improved stress distribution and reduced the stresses transferred to the underlying sub-ballast layer.

It is noteworthy that the pressure plates only measure the mean stresses within their surface areas, and therefore the concentrations of stress due to the inter-particle contact of sharp edges among the ballast aggregates cannot be captured accurately. To further investigate the stress concentrations, a Stress Sensing Sheet (SSS), having dimensions of: 250 mm wide \times 600 mm long \times 0.1 mm thick was used in these tests. This SSS uses a matrix-based tactile surface sensor with two thin sheets of flexible polyester and conductive silver ink printed on them in rows and columns (Figure 10a). The SSS is connected to a host computer supported by a high speed I-Scan system for data acquisition (Figure 10b). When a load is applied, the upper and lower sensor sheets touch each other and the electrical resistance generated at the contact point of rows and columns is inversely proportional to the normal force applied. Figure 11 shows the stress contours measured underneath the ballast layer ($N=100,000$ cycles) for tests with and without artificial inclusions (tests: T1, T2 and T8) subjected to a 25-tonne

axle load at $f = 15\text{Hz}$. The T1 test (without inclusions) revealed many points of concentrated stress (Figure 11a), which led directly to particle breakage, whereas with geogrid (test T2) and geogrid combined with rubber mat (test T8) the contact area increased and the peak stress decreased (Figures 11b and 11c), leading to a reduction in ballast breakage, as measured after the tests. In fact, only a limited concentration of stress was detected when the geogrid and rubber mat were installed underneath the ballast layer (Figure 11c). The increase in the contact area promoted a more uniform distribution of stresses and the associated reduction in the peak stress (i.e., with geogrid and rubber mat, the peak stress was measured as 97 kPa, compared to 312 kPa with the geogrid only).

4. Numerical simulation using the Discrete Element Method

The Discrete Element Method (DEM) has often been used to study the micro-mechanical behaviour of granular materials [27,50-55]. It enables modelling and studying some features of ballast such as irregularly shaped grains, contact force distributions, particle breakage, particle-geogrid interactions, and coordination numbers, which would be almost impossible to measure experimentally or using other numerical techniques. Since the size, shape, and angularity of grains influence the mechanical response of ballast, a 3D laser scanner (VIVID 910) (accurate to 0.22 mm horizontally, 0.16 mm vertically, and 0.1 mm longitudinally) was used to capture the angularity and shape of ballast aggregates (Figure 12). Randomly selected grains of ballast were scanned through laser lights to build polygonal meshes, and then sub-routines were developed in FISH language to build ballast grains in DEM by connecting many spheres of appropriate sizes and positions together to fill up the mesh.

4.1. DEM for geogrid-reinforced ballast

Modelling a real shape of geogrid in DEM is a challenging task due to its complex geometry and flexibility. In this study, a biaxial geogrid was modelled by bonding a number of spherical balls (radius: $r_b = 2.0\text{ mm} - 4.0\text{ mm}$) together by parallel bonds (Figure 13a). The bond strength corresponds to the geogrid tensile strength, which can be determined by tensile tests. Each bond represents the force and displacement response of a piece of cementitious material with a finite size, deposited between two spheres [56]. These bonds form an elastic interaction between particles that can transmit both forces and moments.

Forces and moments acting on parallel bonds are denoted by \overline{F}_i and \overline{M}_i , and can be resolved into normal and shear components as [51]:

$$\overline{F}_i = \overline{F}_i^n + \overline{F}_i^s \quad (6)$$

$$\bar{M}_i = \bar{M}_i^n + \bar{M}_i^s \quad (7)$$

The contact force-increments occurring over a timestep of Δt are calculated by [51]:

$$\Delta \bar{F}_i^n = (-\bar{k}_n A \Delta U_i^n) n_i \quad (8)$$

$$\Delta \bar{F}_i^s = -\bar{k}_s A \Delta U_i^s \quad (9)$$

The increments in moments are determined by:

$$\Delta \bar{M}_i^n = (-\bar{k}_s J \Delta \theta_i^n) n_i \quad (10)$$

$$\Delta \bar{M}_i^s = -\bar{k}_n I \Delta \theta_i^s \quad (11)$$

$$\text{with, } \Delta \theta_i = (\omega_i^{[B]} - \omega_i^{[A]}) \Delta t$$

where, ΔU_i^n and ΔU_i^s are the normal and shear relative displacement increments, respectively; $\Delta \theta_i^n$ and $\Delta \theta_i^s$ are the normal and shear relative rotation increments, respectively; A , I , and J are the area, moment of inertia, and polar moment of the parallel bond cross-section, respectively, defined as:

$$A = \pi \bar{R}^2; \quad I = \frac{1}{2} \pi \bar{R}^4 \quad \text{and} \quad J = \frac{1}{4} \pi \bar{R}^4; \quad (12)$$

The maximum shear and normal stresses acting on the bond are calculated as:

$$\tau_{max} = \frac{|\bar{F}_i^s|}{A} + \frac{|\bar{M}_i^n|}{J} \bar{R} \quad (13)$$

$$\sigma_{max} = \frac{-\bar{F}_i^n}{A} + \frac{|\bar{M}_i^s|}{I} \bar{R} \quad (14)$$

If either of these maximum stresses exceeds its corresponding bond strengths, the parallel bond breaks, corresponding to the breakage of the geogrid. The tensile strength of the parallel bonds for the geogrid was calibrated based on tensile test results (Figure 13), whereas the shear strength of the parallel bonds was determined based on Equations 13-14.

4.2. Determining the model parameters

Micro-mechanical parameters of geogrids were determined from the calibration of tensile tests, as shown in Figure 13a. Simulated geogrids were fixed at one end, while the other end was pulled with increasing load until the tensile strain was around $\varepsilon_l = 8\%$. Field measurements indicate the geogrid tensile strains barely exceed 5% [49]. DEM simulations of tensile tests for geogrid were carried out and the tensile load-strain responses were compared with the results obtained experimentally, where Fig. 13b shows an acceptable agreement between the DEM simulation and the laboratory results. A

set of micromechanics parameters (Table 4) adopted for modelling the geogrid was then established for the current DEM analysis. The contact bonds were used for simulating geogrids only where the bond strengths correspond to the geogrid's tensile strength in the elastic range, as determined from the tensile tests.

Parameters used to simulate granular aggregates in DEM were selected by calibrating the DEM-based shear stress-strain responses of ballast with the laboratory measurements from large-scale direct shear tests. An initial set of parameters adopted from literature was used to simulate the shear tests of ballast in DEM [3,57-62]. These parameters were then varied interactively until the predicted shear stress-strain responses corroborated with those measured experimentally. Once a given set of micro-mechanical parameters had been calibrated (Table 4), these parameters were then used to simulate the PSPTA tests for ballast (with and without geogrid) subjected to cyclic loading. It should be noted that the contact stiffness values used for ballast particles (normal stiffness, $k_n = 8.52 \times 10^8$ N/m and shear stiffness, $k_s = 4.26 \times 10^8$ N/m) are different from those adopted in previous studies because this study involved fresh ballast aggregates, not fouled or recycled ballast as simulated elsewhere.

4.3. Modelling geogrid-reinforced ballast in PSPTA tests

Following the process carried out in the laboratory, a DEM model of the large-scale PSPTA was developed. The capping layer was simulated in DEM using 5 mm diameter spheres to fill up a 150 mm thick layer, as in the laboratory experiments. A layer of geogrid was then placed on the top surface of the capping, followed by a 300 mm thick layer of ballast. Cyclic loads were then applied onto the sleeper and the model was run up to $N=10,000$ cycles. During this simulation the positions of the sleeper and vertical walls were recorded so that the settlement and lateral displacement of the ballast assembly could be captured. Figure 14 compares the settlement and lateral displacement predicted by the DEM model with those measured experimentally under different axle loads and a frequency of $f=15$ Hz; note that the DEM analysis could accurately capture the permanent deformation of ballast subjected to cyclic loading. The DEM simulations also confirmed that the increased axle load intensified the deformation of the ballast. The breakage of particles has not been captured by the current DEM model; however, the micro-mechanical parameters (Table 4) have been carefully calibrated with the laboratory test data. As a result, the DEM model has reasonably captured the load-deformation responses of the ballast assembly.

4.4. Contact force distribution and geogrid deformation

Figure 15 illustrates the contact force distributions of ballast assemblies with and without geogrid captured at $N=1000$ and $N=5000$ cycles from the DEM model. The contact forces between particles

are plotted as lines whose thickness is proportional to the magnitude of these forces. For clarity, only those contact forces which are higher than the average contact force in the assembly are plotted. Fundamentally, an increase in the load cycle resulted in denser contact force chains and increased maximum contact force (P_{max}). Compared to the unreinforced ballast, the geogrid-reinforced ballast assembly exhibited a higher number of contact forces (N_C), but a smaller magnitude of maximum forces (e.g., $N_C = 97,523$ contacts and $P_{max} = 1208$ N for reinforced ballast, compared to $N_C = 92,781$ contacts and $P_{max} = 1312$ N for unreinforced ballast, at $N=1000$ cycles). The reduction in the magnitude of maximum contact forces (P_{max}) due to the presence of the reinforcement justifies the reduction in ballast breakage measured in the laboratory. There was an increased contact at the interface between the ballast and the geogrid reflected by a much larger number of contact forces N_C . The mobilisation of a larger number of contact forces within the geogrid-reinforced ballast assembly is related to the ballast–geogrid interlock that governs the interaction between them [63,64].

Observations made after each laboratory test showed that the geogrid deformed and some ribs were bent and twisted away from their original positions. Figure 16 shows the typical deformed shapes of the geogrids captured in DEM when subjected to 25-tonne and 35-tonne axle loads. Previous laboratory and field studies [49] have also shown that the mobilised strains in geogrids are relatively small, and the geogrids do not generally fail due to shear deformation.

5. Conclusions

This paper investigated how different artificial inclusions improved the performance of ballast under heavy-haul cyclic loading. Large-scale laboratory tests were carried out using the Process Simulation Prismatic Triaxial Apparatus. Two types of geosynthetics and a rubber mat made from scrap tyres were used in the laboratory tests, which were performed under axle loads of $F_{axle} = 25$ -tonne and 35-tonne and frequencies of $f=15$ Hz and 25 Hz to simulate typical Australian freight trains. Corresponding numerical simulations were then carried out using the discrete element method (DEM) to investigate the interaction between the aggregates and geogrid. The following conclusions can be drawn from this study:

- The inclusion of geogrids significantly decreased the permanent deformations of ballast under cyclic loading conditions. Indeed, the geogrid reduced the ε_{vol} by about 19-33% and the ε_s from approximately 17.2% to 29.1%. Subjected to 25-tonne axle load and under a frequency of $f=25$ Hz and without geogrid, the ballast aggregates experienced the highest ε_{vol} and ε_s of about 13.5% and 10.1%, respectively. However, with the

inclusion of a geogrid (GGR) the volumetric strain (ε_{vol}) and shear strain (ε_s) were measured as 11.8% and 8.4%, respectively.

- Regarding the resilient modulus of ballast (M_R), there was a large increase in M_R within the first $N=100,000$ cycles, but then the increase in M_R became marginal and remained relatively unchanged towards the end of the test. For a given applied loading and frequency, the inclusion of geogrid resulted in an increase in M_R . Moreover, under $F_{axle}=25$ -tonne and $f=15$ Hz, the combined geogrid and rubber mat provided the maximum reduction in ballast breakage of $R_{BBI} = 17.74\%$, whereas the geogrid and geocomposite reduced ballast breakage by about $R_{BBI} = 8.06\%$ and $R_{BBI} = 6.45\%$, respectively.
- The vertical stress (σ_v) decreased with the depth of the test chamber where the σ_v values measured at the capping layer were approximately 95 kPa and 210 kPa under 25-tonne and 35-tonne axle loads, respectively. The inclusion of a geogrid at the interface between the ballast and capping layers led to a more effective reduction in the vertical stresses transferred to the sub-ballast in comparison with that for the unreinforced ballast assembly.
- The beneficial effect of geogrid reinforcement was further validated through the numerical model. The DEM simulations showed that the number of contact forces in the geogrid-reinforced ballast exceeded that in the unreinforced ballast assembly due to the interlocking between the geogrid and surrounding ballast grains that partially carried and transmitted contact forces across the assembly.

The outcomes of this study are expected to contribute to better design solutions and revised specifications considering the use of artificial inclusions for enhanced track performance. The improved resiliency of geogrid-reinforced tracks (increased resilient modulus, M_R) along with the reduced long-term ballast deformation and breakage will potentially increase track longevity, leading to extended maintenance cycles and reduced operational costs, while also contributing to a more favourable carbon footprint.

Acknowledgements

The authors would like to thank the Rail Manufacturing CRC, Foundation QA, and Global Synthetics (c/o Mr Amir Shahkolahi) for providing the financial support required to carry out this Research Project (Project R2.5.2). The support from the ARC-Industrial Transformation Training Centre for Advanced Technologies in Rail Track Infrastructure (IC170100006) is also acknowledged. The authors are thankful to Prof Cholachat Rujikiatkamjorn, Dr Chamindi Jayasuriya, Mr Cameron Neilson and Mr Ritchie McLean for their assistance in various phases of the Project. The third author wishes to acknowledge the financial support by: Project PTDC/ECI-EGC/30452/2017 - POCI-01-0145-FEDER-030452 - funded by FEDER funds through COMPETE2020 - Programa Operacional Competitividade e Internacionalização (POCI) and by national funds (PIDDAC) through FCT/MCTES; and Programmatic funding - UIDP/04708/2020 of the CONSTRUCT - Instituto de I&D em Estruturas e Construções - funded by national funds through the FCT/MCTES (PIDDAC).

References

- [1] Selig ET, Waters JM. Track geotechnology and substructure management. London: Thomas Telford; 1994.
- [2] Sayeed MA, Shahin MA. Three-dimensional numerical modelling of ballasted railway track foundations for high-speed trains with special reference to critical speed. *Transp. Geotech.* 2016;6:55-65.
- [3] Tutumluer E, Huang H, Bian X. Geogrid-aggregate interlock mechanism investigated through aggregate imaging-based discrete element modeling approach. *Int. J. Geomech.* 2012;12(4):391-398.
- [4] Shin EC, Kim DH, Das BM. Geogrid-reinforced railroad bed settlement due to cyclic load. *Geotech. Geol. Eng.* 2002;20:261-271.
- [5] Olivier B, Connolly DP, Alves Costa P, et al. The effect of embankment on high speed rail ground vibrations. *Int. J. Rail Transp.* 2016;4(4):229-246.
- [6] Indraratna B, Ngo T, Ferreira F, et al. Laboratory examination of ballast deformation and degradation under impact loads with synthetic inclusions. *Transp. Geotech.* 2020;25:100406.
- [7] Indraratna B, Nimbalkar SS, Ngo NT, et al. Performance improvement of rail track substructure using artificial inclusions: Experimental and numerical studies. *Transp. Geotech.* 2016;8:69-85.
- [8] Li D, Hyslip J, Sussmann T, et al. *Railway geotechnics*. CRC Press; 2015.
- [9] Li L, Liu W, Ma M, et al. Research on the dynamic behaviour of the railway ballast assembly subject to the low loading condition based on a tridimensional DEM-FDM coupled approach. *Constr Build Mater.* 2019;218:135-149.
- [10] Navaratnarajah SK, Indraratna B, Ngo NT. Influence of under sleeper pads on ballast behavior under cyclic loading: Experimental and numerical studies. *J. Geotech. Geoenviron. Eng.* 2018;144(9).

- [11] Le Pen L, Milne D, Thompson D, et al. Evaluating railway track support stiffness from trackside measurements in the absence of wheel load data. *Can. Geotech. J.* 2016;53(7):1156-1166.
- [12] Powrie W, Yang LA, Clayton CRI. Stress changes in the ground below ballasted railway track during train passage. *Proc Inst Mech Eng F J Rail Rapid Transit.* 2007:247-261.
- [13] Ngo NT, Indraratna B, Rujikiatkamjorn C. Stabilisation of track substructure with geoinclusions – experimental evidence and DEM simulation. *Int. J. Rail Transp.* 2017;5(2):63-86.
- [14] Danesh A, Palassi M, Mirghasemi AA. Evaluating the influence of ballast degradation on its shear behaviour. *Int. J. Rail Transp.* 2018;6(3):145-162.
- [15] Chen R, Chen J, Zhao X, et al. Cumulative settlement of track subgrade in high-speed railway under varying water levels. *Int. J. Rail Transp.* 2014;2(4):205-220.
- [16] Ngo NT, Indraratna B, Ferreira FB, et al. Improved performance of geosynthetics enhanced ballast: Laboratory and numerical studies. *Proc. Inst. Civ. Eng.: Ground Improv.* 2018;171(4):202-222.
- [17] Haeri SM, Noorzad R, Oskoorouchi AM. Effect of geotextile reinforcement on the mechanical behavior of sand. *Geotext. Geomembr.* 2000;18:385-402.
- [18] Kwon J, Penman J. The use of biaxial geogrids for enhancing the performance of sub-ballast and ballast layers-previous experience and research. *Proceedings of Bearing Capacity of Road, Railways and Airfields.* 2009: 1321-1330.
- [19] Brown SF, Thom NH, Kwan J, editors. Optimising the geogrid reinforcement of rail track ballast. *Proceedings of Railfound Conference.* 2006: 346-354.
- [20] Leng J, Gabr MA. Deformation-resistance model for geogrid-reinforced. *Transp. Res. Rec.* 2006;1975:146-154.
- [21] Zheng JJ, Chen BG, Lu YE, et al. The performance of an embankment on soft ground reinforced with geosynthetics and pile walls. *Geosynth. Int.* 2009;16(3):173–182.
- [22] Fernandes G, Palmeira EM, Gomes RC. Performance of geosynthetic-reinforced alternative sub-ballast material in a railway track. *Geosynth. Int.* 2008;15(5):311-321.
- [23] Magnani HO, Almeida MSS, Ehrlich M. Behaviour of two reinforced test embankments on soft clay. *Geosynth. Int.* 2009;16(3):127–138.
- [24] Liu C-N, Ho Y-H, Huang J-W. Large scale direct shear tests of soil/PET-yarn geogrid interfaces. *Geotext. Geomembr.* 2009;27(1):19-30.
- [25] Bathurst RJ, Raymond GP. Geogrid reinforcement of ballasted track. *Transp. Res. Rec.* 1987;1153:8-14.
- [26] Brown SF, Kwan J, Thom NH. Identifying the key parameters that influence geogrid reinforcement of railway ballast. *Geotext. Geomembr.* 2007;25(6):326-335.
- [27] McDowell GR, Harireche O, Konietzky H, et al. Discrete element modelling of geogrid-reinforced aggregates. *Proc. Inst. Civ. Eng.: Geotech. Eng.* 2006;159(1):35-48.
- [28] Penman J, Priest DJ. The use of geogrids in railroad applications. *Proceedings of CE News Professional Development Series.* 2009.

- [29] Walls JC, Galbreath LL, editors. Railroad ballast reinforcement subjected to repeated load. Proceedings of Geosynthetics '87 Conference. 1987: 38-45.
- [30] Horníček L, Tyc P, Lidmila M, et al. An investigation of the effect of under-ballast reinforcing geogrids in laboratory and operating conditions. Proc Inst Mech Eng F J Rail Rapid Transit. 2010;224(4):269-277.
- [31] Esmaeili M, Naderi B, Neyestanaki HK, et al. Investigating the effect of geogrid on stabilization of high railway embankments. Soils Found. 2018;58(2):319-332.
- [32] Bergado DT, Teerawattanasuk C. 2D and 3D numerical simulations of reinforced embankments on soft ground. Geotext. Geomembr. 2008;26(1):39-55.
- [33] DeMerchant MR, Valsangkar AJ, Schriver AB. Plate load tests on geogrid-reinforced expanded shale lightweight aggregate. Geotext. Geomembr. 2002;20(3):173-190.
- [34] Duncan-Williams E, Attoh-Okine NO. Effect of geogrid in granular base strength - An experimental investigation. Constr Build Mater. 2008;22(11):2180-2184.
- [35] Phanikumar BR, Prasad R, Singh A. Compressive load response of geogrid-reinforced fine, medium and coarse sands. Geotext. Geomembr. 2009;27(3):183-186.
- [36] Frankowska KK. Influence of geosynthetic reinforcement on the load-settlement characteristics of two-layer subgrade. Geotext. Geomembr. 2007;25:366-376.
- [37] Hussaini SKK, Indraratna B, Vinod JS. A laboratory investigation to assess the functioning of railway ballast with and without geogrids. Transp. Geotech.. 2016;6:45-54.
- [38] Zhang X, Zhao C, Zhai W. Dynamic behavior analysis of high-speed railway ballast under moving vehicle loads using discrete element method. Int. J. Geomech. 2017;17(7):04016157.
- [39] Ngo NT, Indraratna B, Rujikiatkamjorn C. DEM simulation of the behaviour of geogrid stabilised ballast fouled with coal. Comput Geotech. 2014;55:224-231.
- [40] Leng J. Characteristics and behavior of geogrid-reinforced aggregate under cyclic load. PhD Thesis, North Carolina State University, USA; 2002.
- [41] Han J, Bhandari A, Wang F. DEM analysis of stresses and deformations of geogrid-reinforced embankments over piles. Int. J. Geomech. 2011;12(4):340-350
- [42] Tran VDH, Meguid MA, Chouinard LE. A finite–discrete element framework for the 3D modeling of geogrid–soil interaction under pullout loading conditions. Geotext. Geomembr. 2013;37:1-9.
- [43] Sugimoto M, Alagiyawanna AMN. Pullout behavior of geogrid by test and numerical analysis. J. Geotech. Geoenviron. Eng. 2003;129(4):361-371.
- [44] Gundavaram D, Hussaini SKK. Polyurethane-based stabilization of railroad ballast – a critical review. Int. J. Rail Transp. 2019;7(3):219-240.
- [45] AS 2758.7. Aggregates and rock for engineering purposes, Part 7: Railway ballast. Sydney, NSW, Australia: Standards Australia; 2015.
- [46] ARTC ETM-08-01. Earthworks, formation and capping material. Australia: Australian Rail Track Corporation Limited (ARTC); 2010.

- [47] Indraratna, B, Ngo T, Ferreira FB, et al. Large-scale testing facility for heavy haul track. *Transp. Geotech.*. 2021;28:100517.
- [48] Indraratna B, Lackenby J, Christie D. Effect of confining pressure on the degradation of ballast under cyclic loading. *Géotechnique*. 2005;55(4):325–328.
- [49] Indraratna B, Nimbalkar S, Neville T. Performance assessment of reinforced ballasted rail track. *Proc. Inst. Civ. Eng.: Ground Improv.* 2014;167(1):24-34.
- [50] Cundall PA, Strack ODL. A discrete numerical model for granular assemblies. *Géotechnique*. 1979;29(1):47-65.
- [51] Cheng YP, Bolton MD, Nakata Y. Crushing and plastic deformation of soils simulated using DEM. *Géotechnique*. 2004;54(2):131-141.
- [52] Huang H, Tutumluer E. Discrete Element Modeling for fouled railroad ballast. *Constr Build Mater.* 2011;25:3306-3312.
- [53] Indraratna B, Ngo NT, Rujikiatkamjorn C, et al. Behaviour of fresh and fouled railway ballast subjected to direct shear testing - a discrete element simulation. *Int. J. Geomech.* 2014;14(1):34-44.
- [54] Tutumluer E, Qian Y, Hashash YMA, et al. Discrete element modelling of ballasted track deformation behaviour. *Int. J. Rail Transp.* 2013;1(1-2):57-73.
- [55] Guo, Y, Zhao C, Markine V, et al. Discrete element modelling of railway ballast performance considering particle shape and rolling resistance. *J. Railw. Eng.* 2020;28(4):382-407.
- [56] Itasca. Particle flow code in three dimensions (PFC3D). Minnesota: Itasca Consulting Group, Inc; 2016.
- [57] Lobo-Guerrero S, Vallejo LE. Discrete element method analysis of railtrack ballast degradation during cyclic loading. *Granul. Matter.* 2006;8(3-4):195-204.
- [58] Lu M, McDowell GR. Discrete element modelling of railway ballast under monotonic and cyclic triaxial loading. *Géotechnique*. 2010;60(6):459-467.
- [59] Guo Y, Zhao C, Markine V, et al. Calibration for discrete element modelling of railway ballast: A review. *Transp. Geotech.*. 2020;23:100341.
- [60] Huang ZY, Yang ZX, Wang ZY. Discrete element modeling of sand behavior in a biaxial shear test. *J. Zhejiang Univ. Sci.* 2008;9(9):1176-1183.
- [61] Suhr B, Marschnig S, Six K. Comparison of two different types of railway ballast in compression and direct shear tests: experimental results and DEM model validation. *Granul. Matter.* 2018;20(4):70-70.
- [62] Guo Y, Zong L, Markine V, et al. Experimental and numerical study on lateral and longitudinal resistance of ballasted track with nailed sleeper. *Int. J. Rail Transp.* 2021:1-19.
- [63] Konietzky H, te Kamp L, Groeger T. Use of DEM to model the interlocking effect of geogrids under static and cyclic loading. *Proceedings of the Numerical Modeling in Micromechanics via Particle Methods.* 2004: 3-11.
- [64] Lim WL, McDowell GR. Discrete element modelling of railway ballast. *Granul. Matter.* 2005;7(1):19-29.

[65] ASTM - D6637. Standard test method for determining the tensile properties of geogrids by the single rib or multi-rib tensile method. Philadelphia, USA: ASTM International; 2011.

[66] DIN 45673–5. Mechanical vibration. Resilient elements used in railway tracks, Part 5: Laboratory test procedures for under-ballast mats. Berlin, Germany: German Institute for Standardisation (DIN); 2010.

Table 1. Physical and mechanical properties of the tested geosynthetics and recycled rubber mat

Properties	Geogrid (GGR)	Geocomposite (GCR)	Rubber mat (RM)
Structure	Biaxial geogrid	Biaxial geogrid + Geotextile	Planar mat
Mass per unit area	240g/m ²	390g/m ²	8230g/m ²
Open area	62.5%	62.5%	-
Geogrid aperture size (MD × CD)	≈31 × 31 mm	≈31 × 31 mm	-
Thickness	≈0.9 mm	≈0.9 mm	10 mm
Tensile strength at 2% strain ^a	17.2 kN/m	24.7 kN/m	25.80 kN/m
Tensile strength at 5% strain ^a	31.3 kN/m	35 kN/m	56.7 kN/m
Peak tensile strength ^a	41.7 kN/m	≥42 kN/m	-
Strain at peak ^a	8.8%	≤10%	56%
Static bedding modulus, C_{stat} ^b	-	-	0.142 (N/m ³)
Dynamic bedding modulus, C_{dyn} ^b	-	-	0.107 (N/m ³)

^a According to ASTM D6637:2011 [65]

^b According to DIN 45673–5:2010 [66]

Table 2. Test program for the large-scale PSPTA

Test No.	Type of artificial inclusion used	Loading frequency, f (Hz)	Axle load, F_{axle} (tonne)	No. cycles, N	Confining pressure, σ_3 (kPa)
T1	None - benchmarking test	15	25	500 000	15
T2	Geogrid - GGR	15	25	500 000	15
T3	None - benchmarking test	15	35	500 000	15
T4	Geogrid - GGR	15	35	500 000	15
T5	None - benchmarking test	25	25	500 000	15
T6	Geogrid - GGR	25	25	500 000	15
T7	Geocomposite - GCR	15	25	500 000	15
T8	GGR + RM (Rubber mat)	15	25	500 000	15

Table 3. Summary of measured ballast breakage for different tests

<i>BBI</i>	Test number							
	T1	T2	T3	T4	T5	T6	T7	T8
Top layer	0.069	0.061	0.102	0.098	0.086	0.075	0.061	0.060
Middle layer	0.055	0.052	0.061	0.059	0.059	0.055	0.054	0.048
Bottom layer	0.061	0.059	0.090	0.075	0.072	0.069	0.059	0.044
Average breakage	0.062	0.057	0.084	0.077	0.072	0.066	0.058	0.051
<i>R_{BBI}</i> (%)		8.06		8.33		8.33	6.45	17.74

Table 4. Micro-mechanical parameters used for the DEM analysis

Parameters	Ballast	Capping	Geogrid
Particle density (kg/m^3)	2700	2350	965
Inter-particle coefficient of friction, μ	0.85	0.75	0.47
Contact normal stiffness, k_n (N/m)	8.52×10^8	2.41×10^8	5.26×10^6
Contact shear stiffness, k_s (N/m)	4.26×10^8	2.41×10^8	2.18×10^6
Contact normal stiffness of wall-particle, k_{n-wall} (N/m)	3.25×10^9	3.25×10^9	3.25×10^9
Shear stiffness of wall of wall-particle, k_{s-wall} (N/m)	3.25×10^9	3.25×10^9	3.25×10^9
Parameter of contact bond normal strength, ϕ_n (kN)			56.8
Parameter of contact bond shear strength, ϕ_s (kN)			56.8
Parallel bond radius multiplier, r_p			0.5
Parallel bond normal stiffness, k_{np} (kPa/m)			6.27×10^7
Parallel bond shear stiffness, k_{sp} (kPa/m)			6.27×10^7
Parallel bond normal strength, σ_{np} (MPa)			297
Parallel bond shear strength, σ_{sp} (MPa)			297

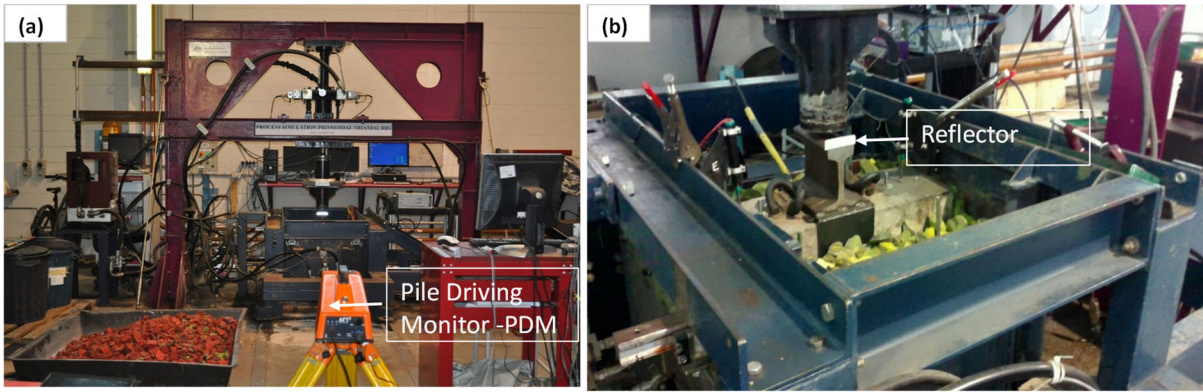


Figure 1. Process Simulation Prismoidal Triaxial Apparatus: (a) general view of the test rig; (b) ballast sample prepared for testing and detail of rail-sleeper assembly

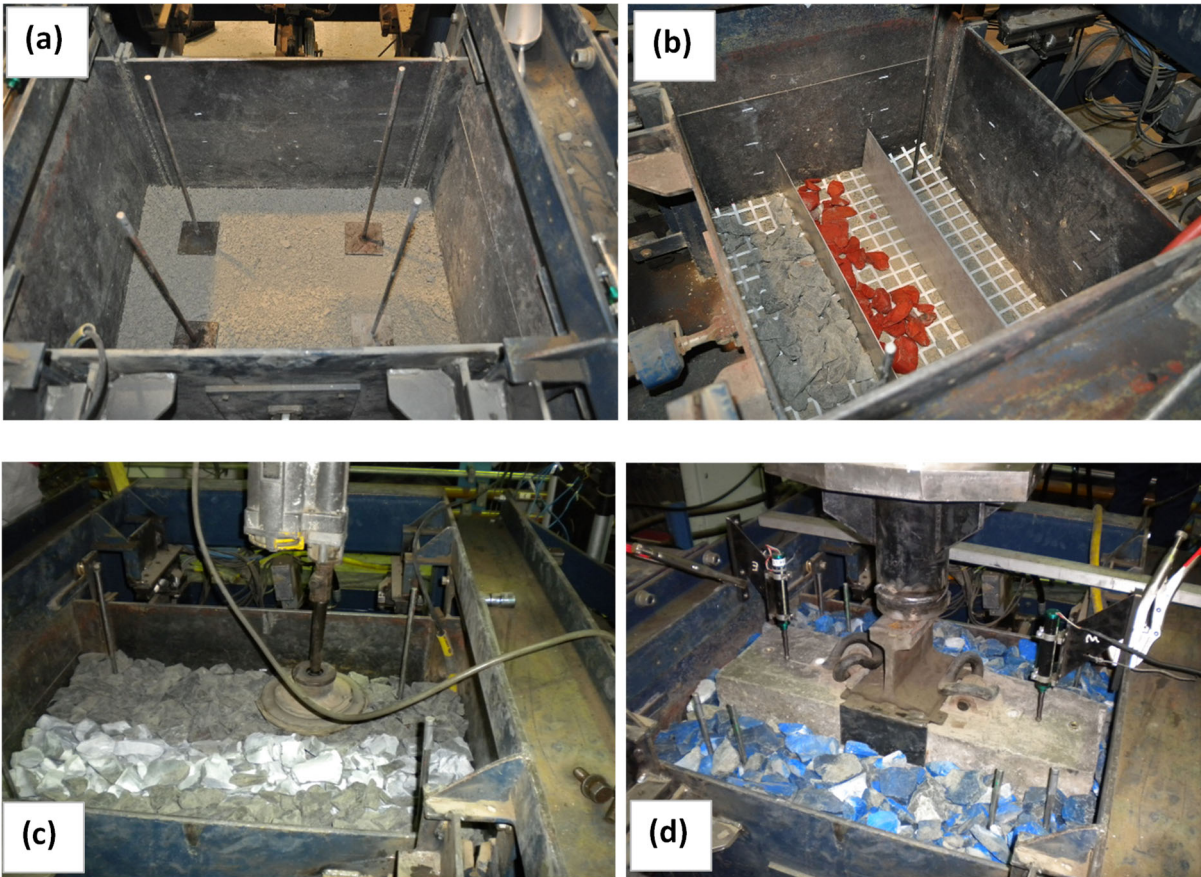


Figure 2. Preparation of the test samples: (a) capping layer after compaction; (b) installation of geogrid reinforcement and bottom ballast layer; (c) compaction of top ballast layer; (d) complete model test with instrumentations

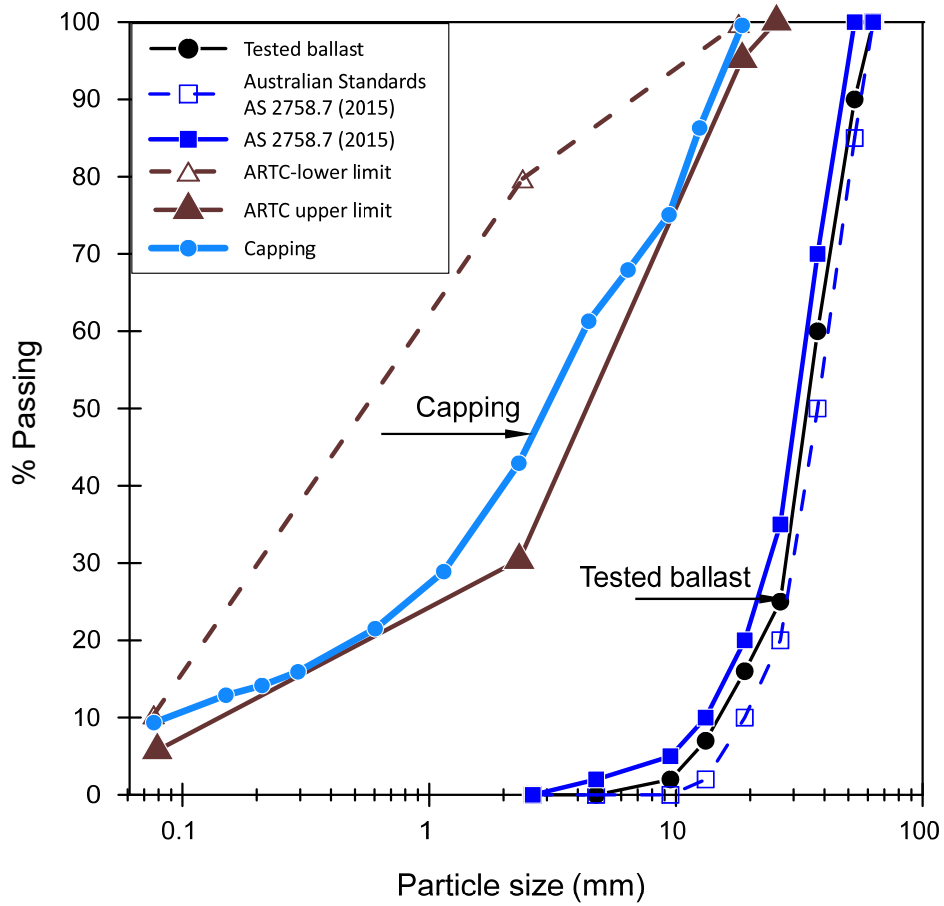


Figure 3. Particle size distribution of ballast and capping materials used in this study and recommended gradation as per the AS 2758.7:2015 [45] and ARTC ETM-08-01:2010 [46].

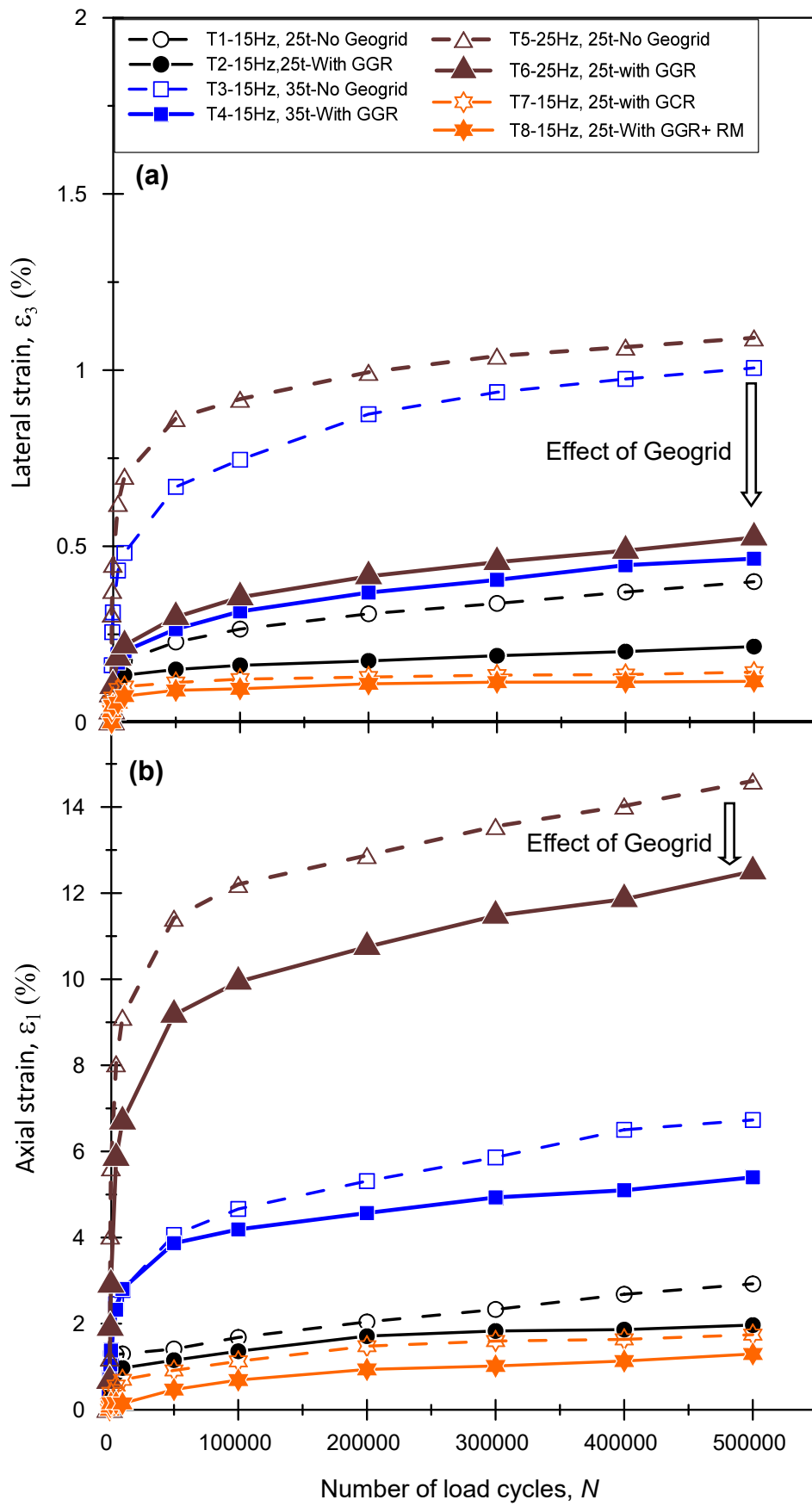


Figure 4. Measured deformation responses of ballast with and without the inclusion of geogrids and recycled rubber mat: (a) lateral strain (ϵ_3) and (b) axial strain (ϵ_1)

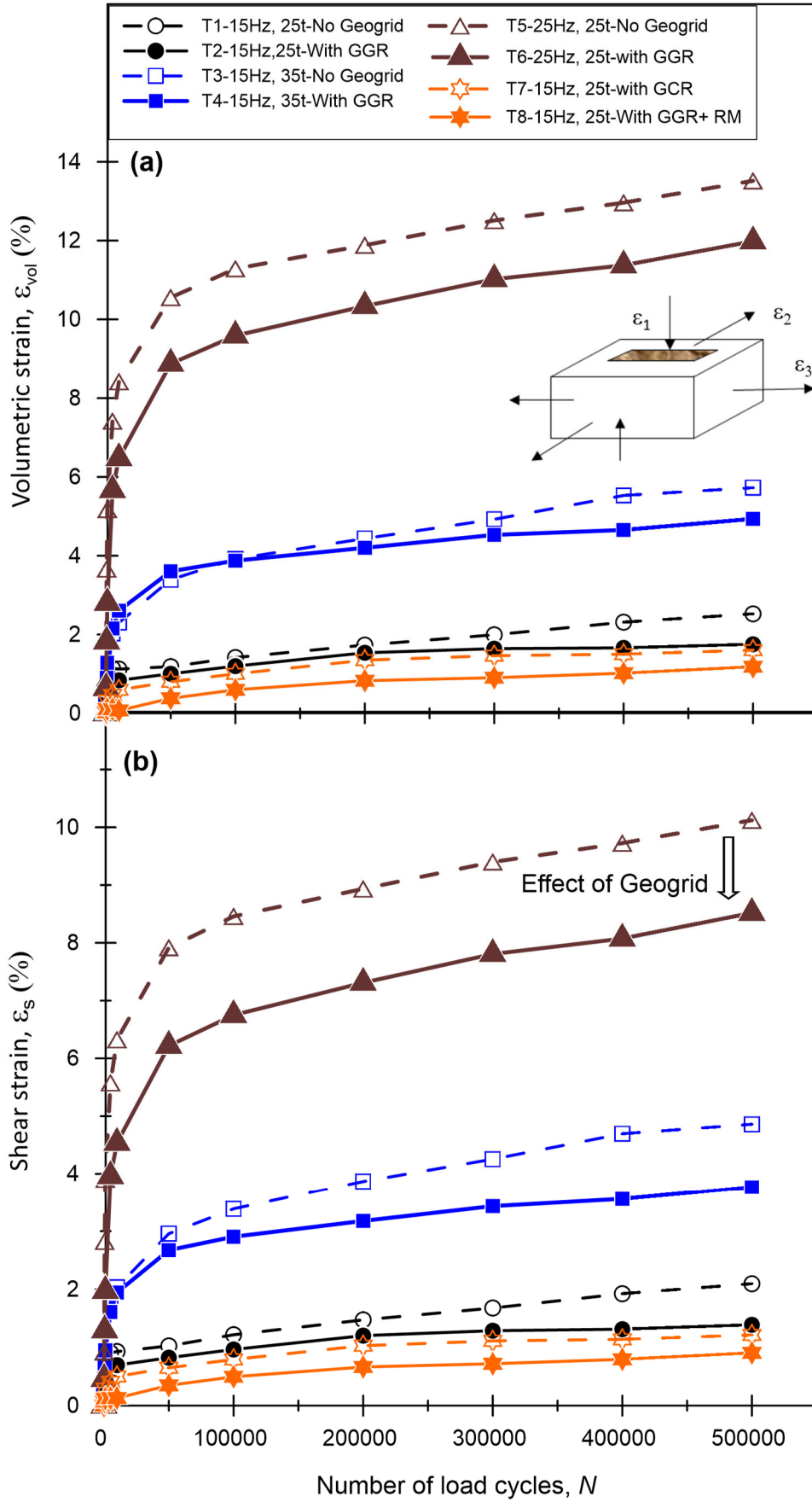


Figure 5. Measured volumetric strain (a) and shear strain (b) of ballast with and without the inclusion of geogrids and recycled rubber mat

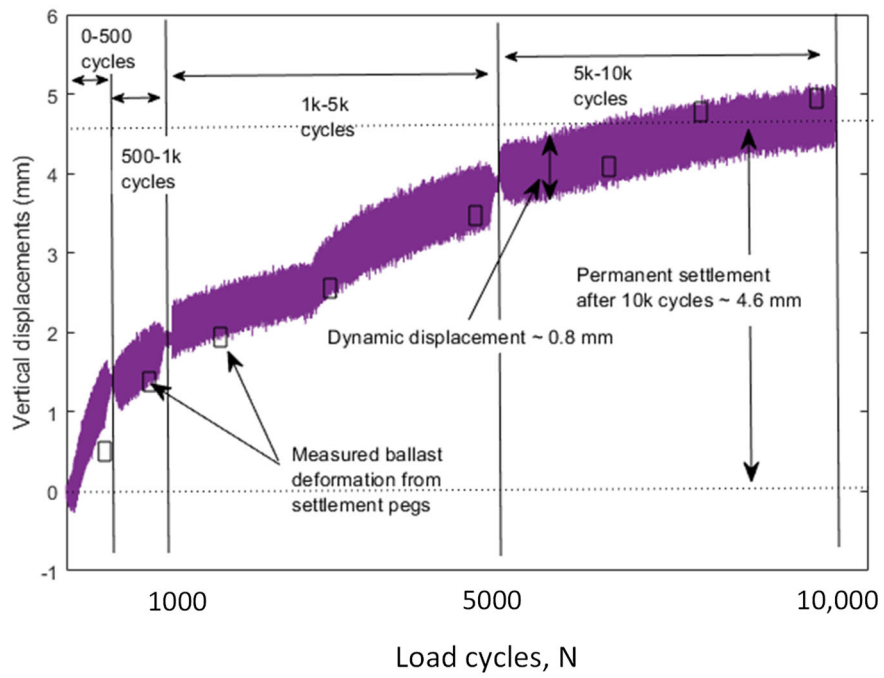


Figure 6. Vertical displacement of the rail recorded by the PDM during test T2

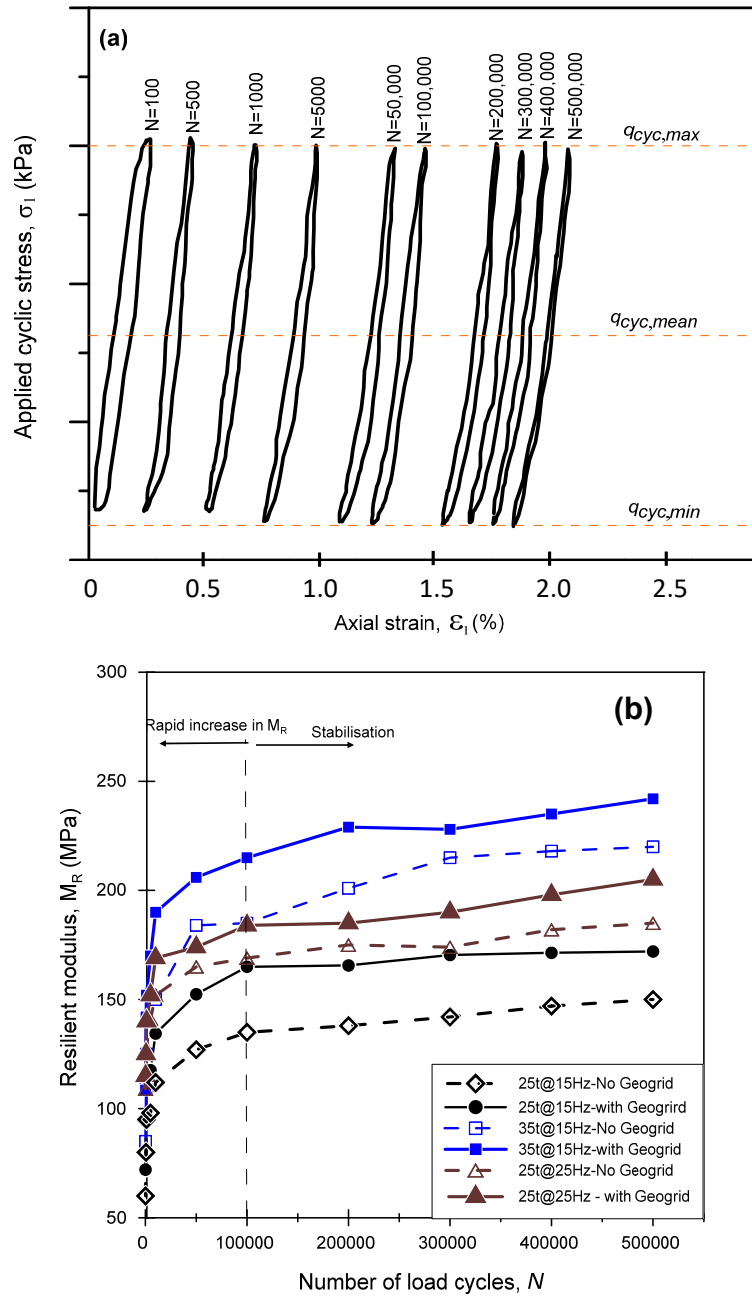


Figure 7. (a) Applied cyclic stress versus axial strain curves at predefined numbers of cycles (test T2) and (b) Measured resilient modulus of ballast (M_R) under different axle loads and frequencies

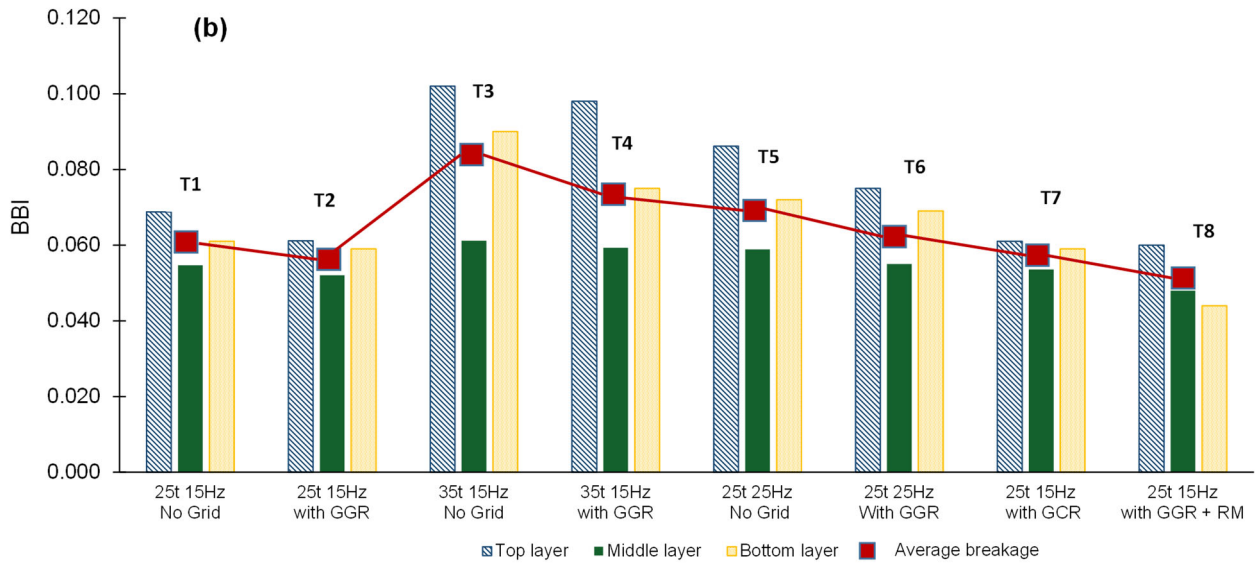
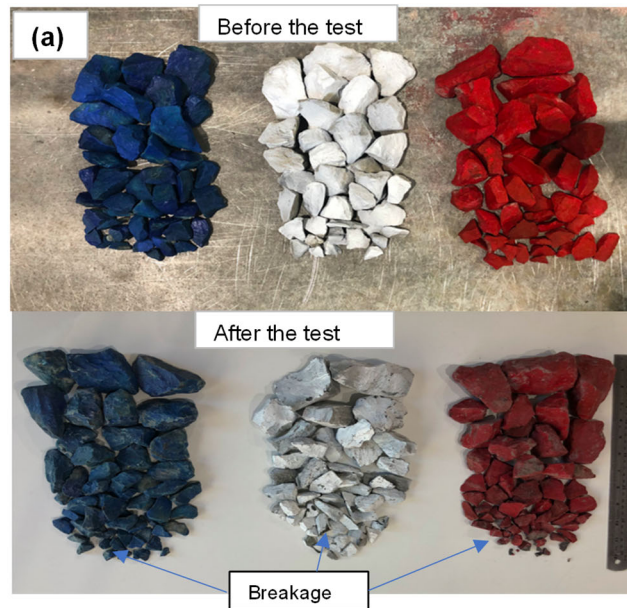


Figure 8. (a) Selected ballast aggregates before and after the test; (b) Measured ballast breakage at different layers of ballast

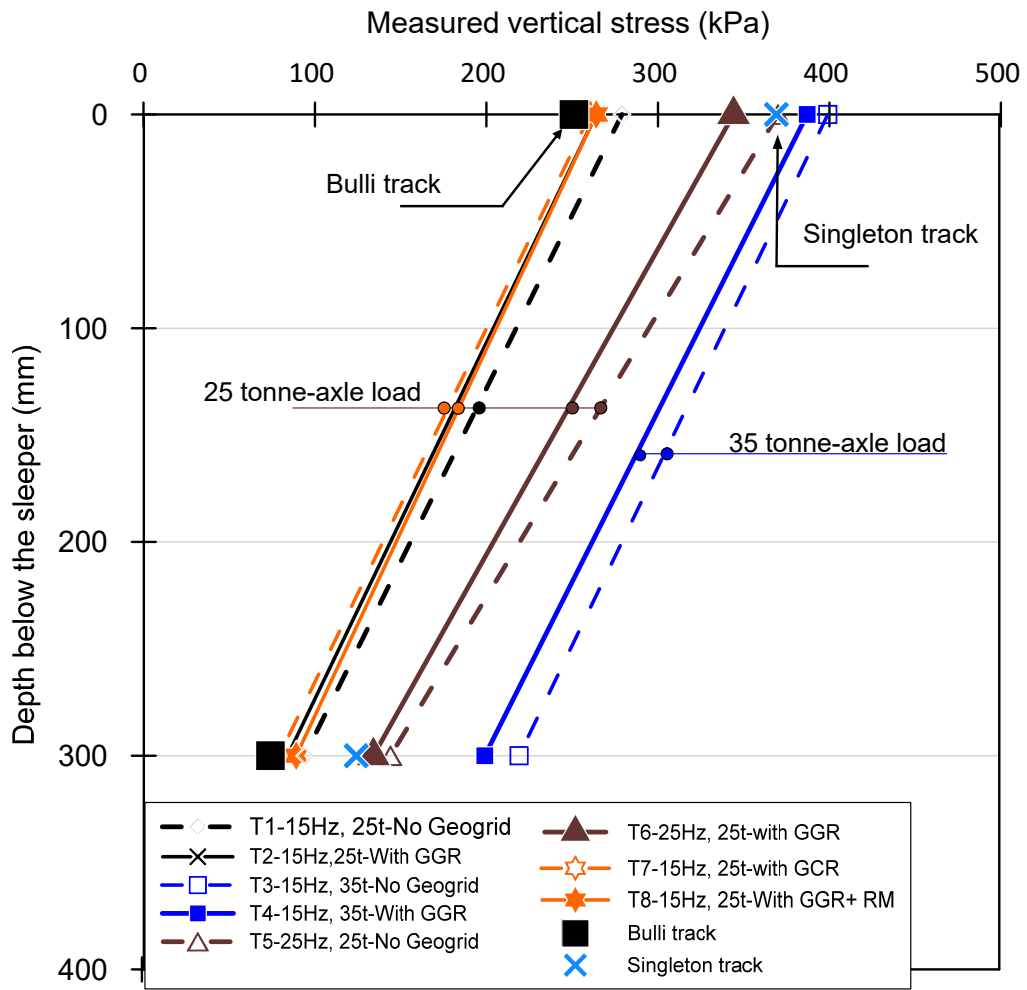


Figure 9. Variations of measured vertical stresses with depth and comparison with field measurements

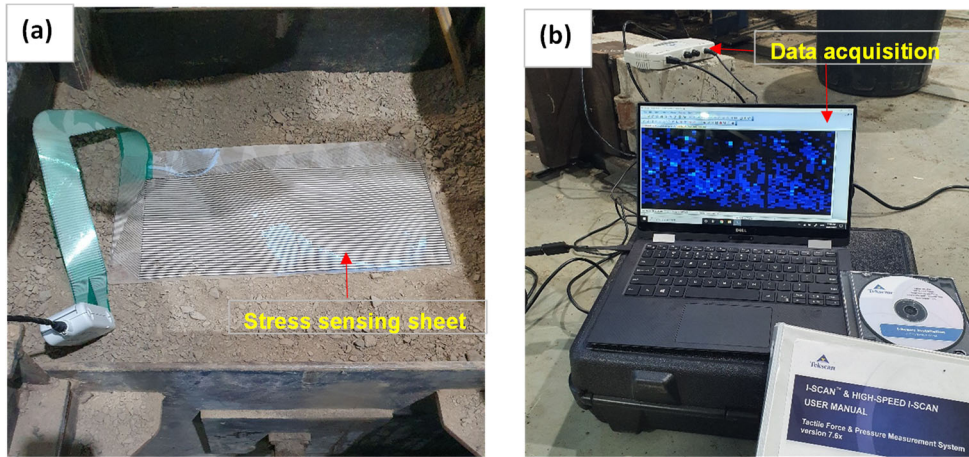


Figure 10. Use of Stress Sensing Sheet (SSS) for detecting stress concentrations: (a) SSS placed on top of the capping layer in the PSPTA; (b) data acquisition software.

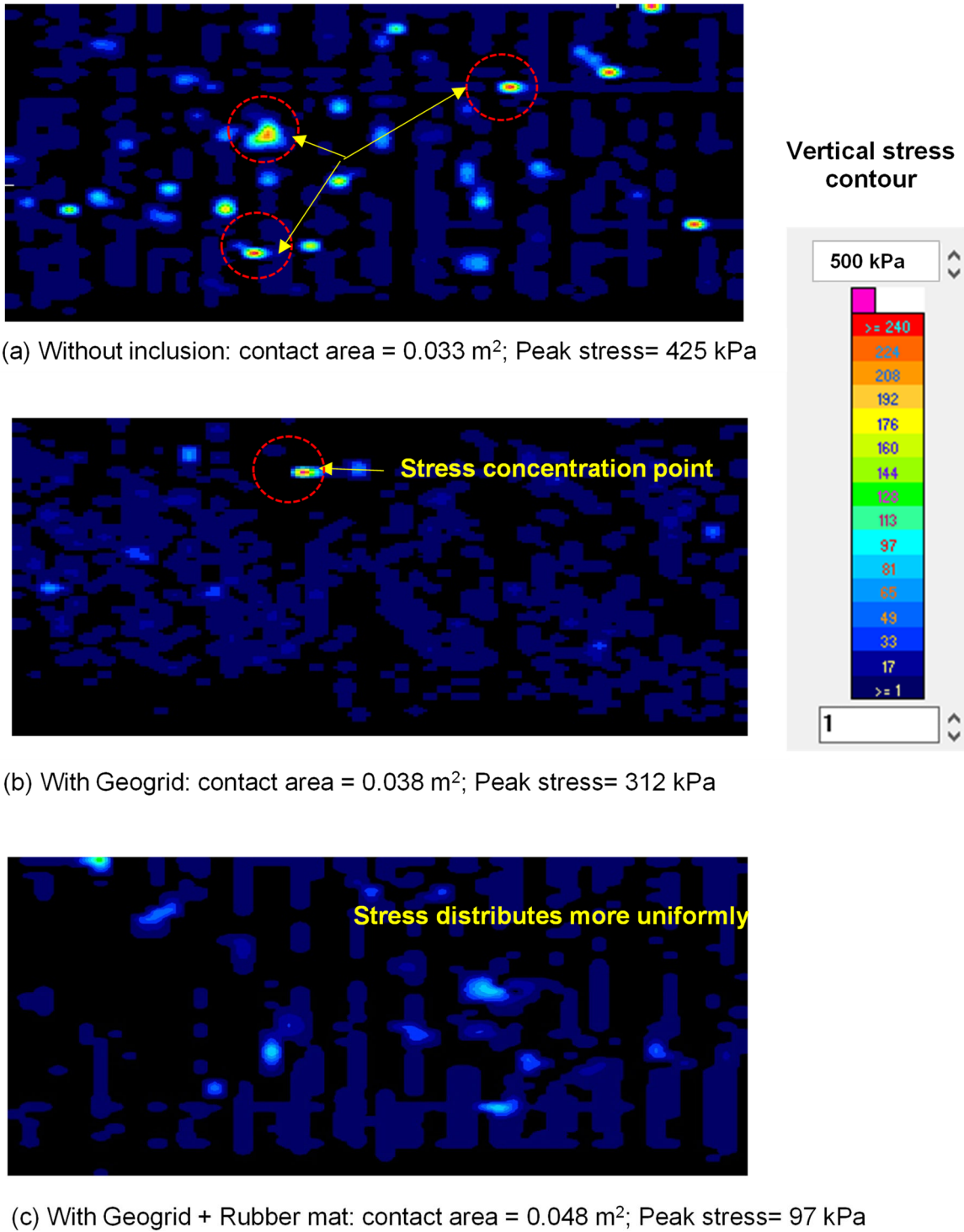


Figure 11. Measured stress distribution at the capping/ballast interface: (a) Without inclusion (b) With a Geogrid; and (c) With a Geogrid + Rubber mat

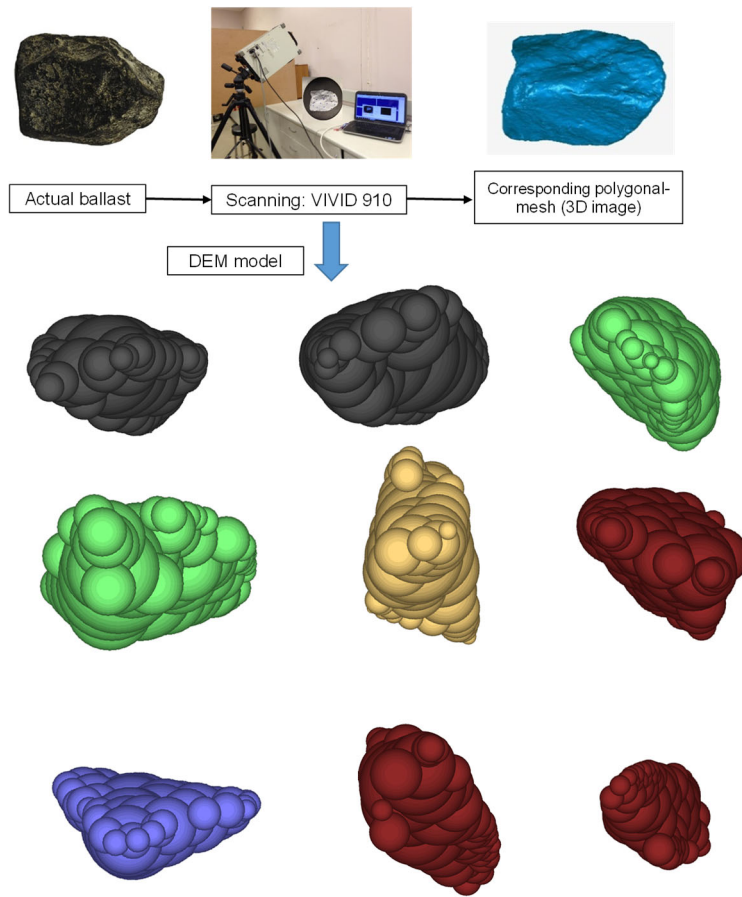
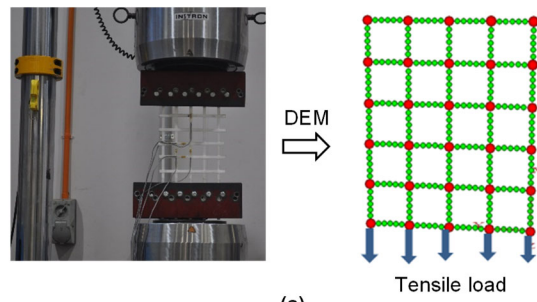
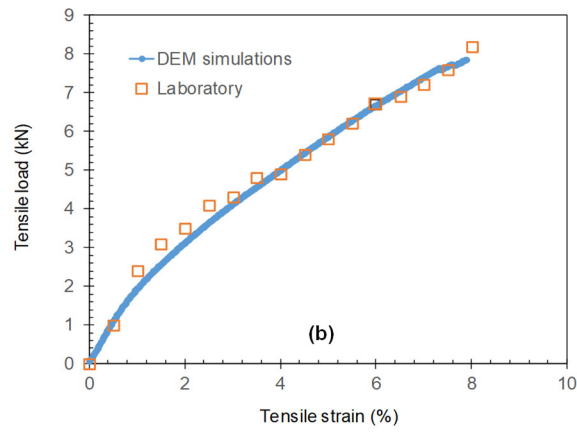


Figure 12. Process of modelling ballast particles in DEM



(a)



(b)

Figure 13. Determination of DEM parameters for the simulated geogrid: (a) Tensile tests; (b) Validation of tensile load-strain responses of geogrid measured from laboratory and DEM simulations

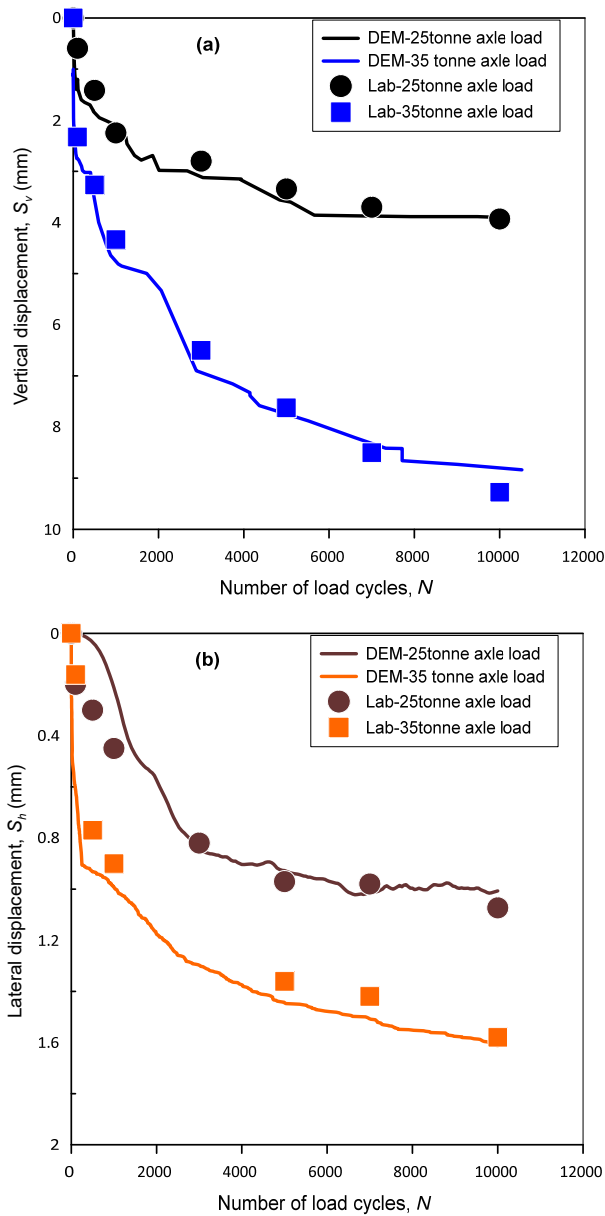
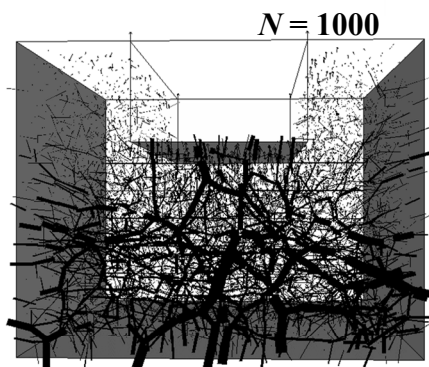
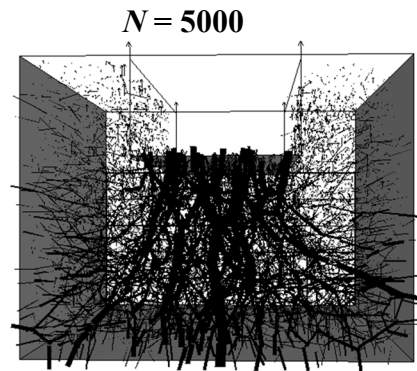


Figure 14. Comparisons of predicted ballast displacements with those measured in the laboratory ($f=15$ Hz): (a) vertical settlement; and (b) lateral displacement.

(a) Without Geogrid

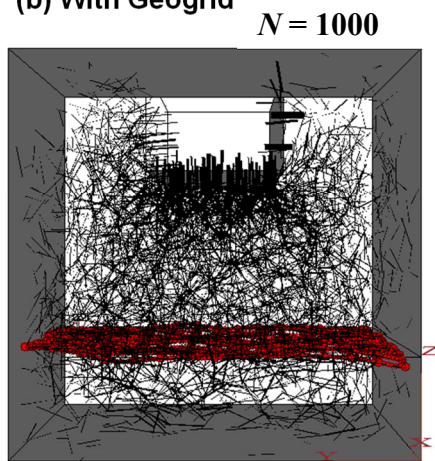


Number of contacts: 92,781
Maximum contact force: 1312 N

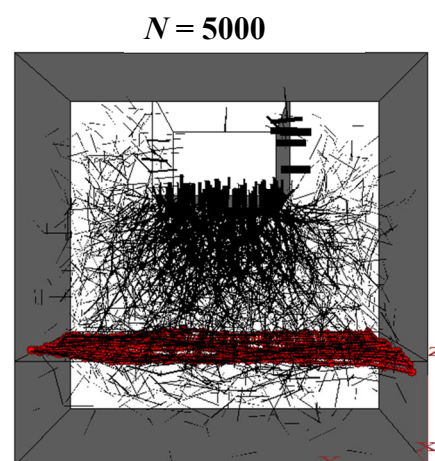


Number of contacts: 96,523
Maximum contact force: 1316 N

(b) With Geogrid



Number of contacts: 97,523
Maximum contact force: 1208 N



Number of contacts: 98,862
Maximum contact force: 1252 N

Figure 15. Contact force distributions captured at $N=1000$ and $N=5000$ load cycles: (a) without geogrid; and (b) with geogrid

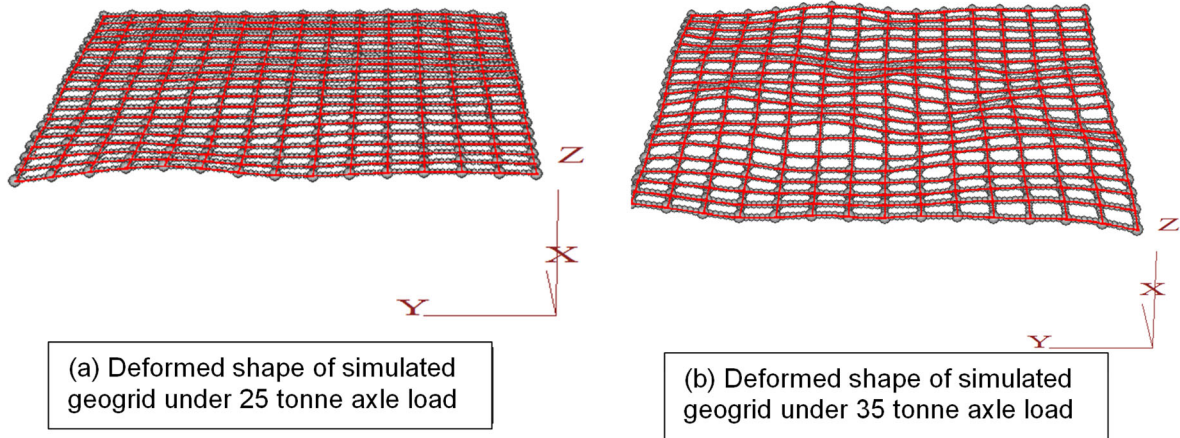


Figure 16. Typical deformed shape of geogrid: (a) 25-tonne axle load; and (b) 35-tonne axle load